Interplay Effects in the Co-Doping of ZnO Nanowires with Al and Ga Using Chemical Bath Deposition

Adrien Baillard, Estelle Appert, Matthieu Weber, Véronique Jacob, Hervé Roussel, Laetitia Rapenne, Odette Chaix-Pluchery, Vincent Consonni

Interplay Effects in the Co-Doping of ZnO Nanowires with Al and Ga Using Chemical Bath Deposition

Adrien Baillard,[1] Estelle Appert,[1] Matthieu Weber,[1] Véronique Jacob,[2] Hervé Roussel,[1] Laetitia Rapenne,[1] Odette Chaix-Pluchery,[1] and Vincent Consonni.[1*]

[1] Université Grenoble Alpes, CNRS, Grenoble INP, LMGP, F-38000 Grenoble, France

[2] Université Grenoble Alpes, CNRS, IRD, Grenoble INP, IGE, F-38000 Grenoble, France

CORRESPONDING AUTHOR FOOTNOTE:

*E-mail: vincent.consonni@grenoble-inp.fr

ABSTRACT

The simultaneous co-doping of ZnO nanowires grown by chemical bath deposition is of high interest for a large number of engineering devices, but the process conditions required and the resulting physicochemical processes are still largely unknown. Herein, we show that the simultaneous co-doping of ZnO nanowires with Al and Ga following the addition of $Al(NO_3)_3$ and $Ga(NO_3)_3$ in the chemical bath operates in a narrow range of conditions in the high pH region, where the adsorption processes of respective $Al(OH)_4^-$ and $Ga(OH)_4^-$ complexes on the positively charged *m*-plane sidewalls are driven by attractive electrostatic forces. The structural morphology and properties of ZnO nanowires are significantly affected by the co-doping and mainly governed by the effect of Al(III) species. The incorporation processes of Al and Ga dopants are characterized by significant interplay effects, and the amount of incorporated Ga dopants into ZnO nanowires is found to be larger than the amount of incorporated Al dopants owing to energetic considerations. The Al and Ga dopants are located in the bulk of ZnO nanowires but a part of Al and Ga lies on their surfaces, their incorporation

process in the bulk being enhanced by thermal annealing under oxygen atmosphere. Eventually, the Al and Ga dopants directly affect the incorporation of hydrogen-related defects, notably by annihilating the formation of V_{Zn}-*n*H defect complexes. These findings present an efficient strategy to proceed with the co-doping of ZnO nanowires grown by chemical bath deposition, opening perspectives to control their electronic structure properties with a higher precision.

KEYWORDS: ZnO nanowires, co-doping, chemical bath deposition.

GRAPHICAL ABSTRACT

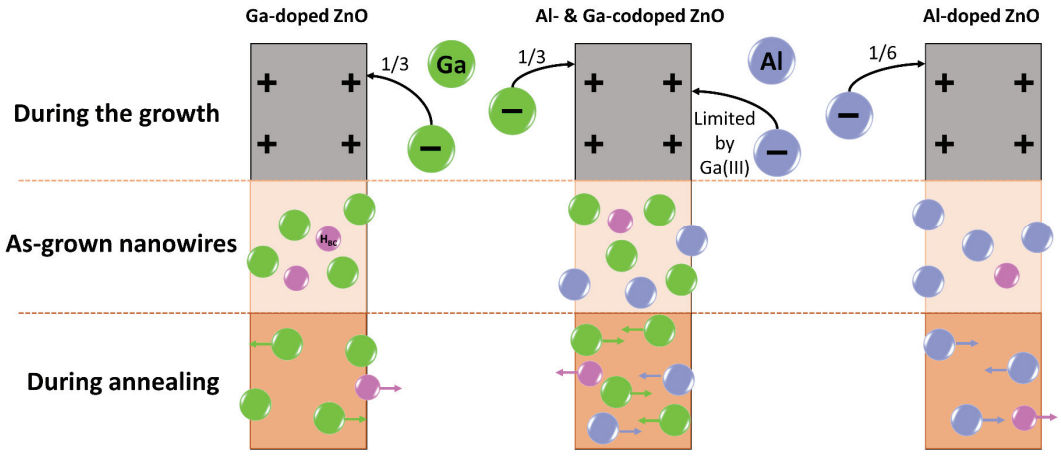

1. INTRODUCTION

ZnO in the form of nanowires (NWs) is one of the most promising sustainable semiconductors owing to its biocompatibility and its attractive physical properties,[1-2] including a direct wide band gap energy, a large exciton binding energy, and a relatively high electron mobility.[3] ZnO NWs can act as building blocks for a wide variety of devices such as light emitting diodes,[4] lasers,[5] UV photodetectors,[6] solar cells,[7] piezoelectric nano-generators,[8] photo-catalysts,[9] gas sensors,[10-11] and biological sensors.[12-13] The chemical bath deposition (CBD) processes offer the possibility to prepare vertically aligned ZnO NWs with a great structural morphology over flexible and rigid substrates[14] and can be compatible with green chemistry.[15] The doping of ZnO NWs grown by CBD deserves a particular attention to optimize and control their optical and electrical properties.[16] Although the doping of ZnO has extensively been investigated theoretically by density-functional theory (DFT) calculations and experimentally in single crystals and thin films grown by vapor phase deposition techniques,[17-18] its implementation during the CBD of ZnO NWs exhibits a couple of specific particularities that are inherent to their formation in an aqueous solution kept at low temperature. In particular, the growth medium in aqueous solution is polar and contains hydrogen and nitrogen, governing the predominant electrostatic forces and affecting the electronic structure properties of ZnO NWs through an effective non-intentional doping, respectively.[19-20]

The use of group III-A dopants such as Al, Ga, and In is known to tune the physical properties of ZnO through an efficient n-type doping.[17-18] To perform the intentional doping of ZnO NWs by CBD, a chemical precursor such as a metal salt containing the dopant is typically employed in addition to a zinc salt and an amine providing Zn(II) species and hydroxide ions, respectively.[21-23] However, the conditions required during the CBD process (*e.g.* pH and concentration of chemical precursors) to ensure the proper doping of ZnO NWs are specific and differs from the widely used conditions. The incorporation of Al and Ga dopants into ZnO NWs has been found to operate in a narrow range of high pH values following attractive electrostatic forces between the anion complexes containing the dopant (*i.e.* $Al(OH)_4^-$ and $Ga(OH)_4^-$) and the positively charged *m*-plane sidewalls.[21-22] The resulting free electron density in ZnO NWs has accordingly been shown to drastically increase following the doping with Al and Ga.[24] These studies have revealed that the implementation of the doping of ZnO NWs by CBD should be optimized for each dopant considered although

some general thermodynamic considerations hold for all dopants. In that way, there could be an opportunity to obtain co-doped ZnO NWs with Al and Ga by optimizing the conditions during the CBD process. In that context, the co-doping of ZnO NWs has emerged as an additional route to further optimize their optical and electrical properties, which is required when they are used as electron transporting materials for nanostructured solar cells[7] or as photo-catalysts[9] for water remediation. While a couple of reports have investigated the co-doping of ZnO thin films[25-28] and the growth of ZnO NWs by CBD on Al- and Ga-codoped ZnO seed layers,[29] the implementation of the co-doping by CBD is still open. Moreover, the massive incorporation of hydrogen during the CBD process of ZnO NWs is expected to interfere with the intentional doping,[20] but this issue has never been explored so far.

In this article, the co-doping of ZnO NWs with Al and Ga by CBD is achieved by simultaneously adding aluminium nitrate and gallium nitrate in the bath. The physicochemical processes operating in aqueous solution are investigated by thermodynamic computations and *in situ* pH measurements. The effect of the simultaneous co-doping on the morphological and structural properties of ZnO NWs as well as on the Al and Ga incorporation mechanisms are studied using field-emission scanning electron microscopy (FESEM), X-ray diffraction (XRD), scanning transmission electron microscopy (STEM), energy-dispersive X-ray spectroscopy (EDX) using TEM, inductively coupled plasma-mass spectrometry (ICP-MS), X-ray photoelectron spectroscopy (XPS), Raman spectroscopy, and UV-Vis-NIR absorption measurements.

2. EXPERIMENTAL DETAILS

2.1. Deposition techniques. (001) silicon wafers and Corning borosilicate glass were used as substrates and previously cleaned in an ultrasonic bath with acetone and isopropyl alcohol to remove the residual contaminants. The polycrystalline ZnO seed layers were deposited by dip coating using a sol-gel process. The chemical precursor solution was composed of 375 mM zinc acetate dihydrate [$Zn(CH_3COO)_2 \cdot 2H_2O$, Sigma-Aldrich] and 375 mM monoethanolamine [MEA, Sigma-Aldrich] mixed in pure ethanol. The substrates were dipped into the solution and gently pulled out at a withdrawal speed of 3.3 $cm.s^{-1}$ under a controlled atmosphere (<15% hygrometry). They were first annealed at 300°C for 10 minutes on a hot plate to evaporate the residual organic compounds and then at 500°C for 1 hour in an oven under air to crystallize the ZnO polycrystalline seed layer. The growth of ZnO NWs was achieved by CBD in a sealed reactor containing a chemical precursor

solution composed of zinc nitrate hexahydrate [$Zn(NO_3)_2 \cdot 6H_2O$, Sigma-Aldrich] and HMTA [$C_6H_{12}N_4$, Sigma-Aldrich] with an equimolar concentration of 30 mM mixed in deionized water. The dopants were intentionally added in the chemical bath using aluminium nitrate nonahydrate [$Al(NO_3)_3 \cdot 9H_2O$, Sigma-Aldrich] and gallium nitrate hydrate [$Ga(NO_3)_3 \cdot xH_2O$, Sigma-Aldrich, with x considered as 8.[30] The total $Al(NO_3)_3$ and $Ga(NO_3)_3$ concentration in the chemical bath was set to 0.9 mM. The $[Al(NO_3)_3]/[Zn(NO_3)_2]$ and $[Ga(NO_3)_3]/[Zn(NO_3)_2]$ ratios were varied as 0%/0% for non-intentionally doped ZnO NWs, 3%/0% for Al-doped ZnO NWs, 2%/1%, 1.5%/1.5%, and 1%/2% for Al- and Ga-codoped ZnO NWs, and 0%/3% for Ga-doped ZnO NWs, respectively. A given volume of deionised water was added in the case of non-intentionally doped ZnO NWs to compensate for the dopant solution volumes. Prior to the growth, ammonia [NH_3, Sigma-Aldrich] with a concentration of 725 mM was added to the chemical bath, resulting in an initial pH at room temperature of approximately 10.9. The sealed reactor was placed for 3 hours in an oven heated at 90 °C. Both the pH and temperature were recorded in an *in situ* manner to follow their variation as CBD proceeds, using an InLab Versatile Pro pH electrode from Mettler Toledo. A thermal annealing at 400°C for 1 hour was eventually performed in a tubular furnace under oxygen atmosphere.

2.2. Characterization techniques. The morphology of ZnO NWs on silicon was assessed with a ZEISS Gemini 300 FESEM instrument using an in-lens detector and an acceleration voltage of 5 keV. The XRD acquisitions were performed with a BRUKER D8 Advance diffractometer using the Cu $K\alpha_1$ radiation according to the Bragg−Brentano configuration. The θ/2θ XRD patterns were collected between 20 and 80° (in 2Theta scale), calibrated with the (004) diffraction peak of Si pointing at $2\Theta = 69.131°$, and refined with Celref 3 software using the 00-036-1451 ICDD file. STEM specimens were prepared by scratching the surface of ZnO NW arrays using a diamond tip and spread on a copper grid. STEM-EDS spectra and maps were collected with a JEOL SDD Centurio detector having a large solid angle of up to 0.98 steradians incorporated in the JEOL 2100F field-emission-gun scanning electron microscope operating at 200 kV and having a 0.2 nm resolution in the scanning mode. The chemical composition was determined with a NexION 1000 PERKIN ELMER ICP-MS instrument. The nebulizer and spray chamber were a MEINHARD plus Glass Type C and Glass Cyclonic at 2°C, respectively. The KED mode was used with He (7% H_2) as collision gas. The glass substrates were dipped into a 0.6% nitric acid solution [HNO_3, Carlo Erba] to dissolve ZnO NWs. The RF power was 1450 W, the KED flow rate was 4 mL/min, and the integration time was set to 10, 10, and 100 ms

for detecting Zn, Ga, and Al, respectively. The PERKIN ELMER reference solutions were diluted to obtain 0.01, 0.1, 0.2, 0.5 and 1 mg/L of Zn, Al, and Ga standards. The analysed solutions were diluted to lie in the calibration range. The solution containing only the glass substrate was previously assayed to make sure that no contaminants are released during the preparation. XPS spectra were collected in ultrahigh vacuum (10^{-8} mbar) and at room temperature with a ThermoScientific K-Alpha spectrometer using a monochromatic Al Kα radiation source (1486.6 eV). The spot size area was adjusted to 400 µm in diameter and the acquisitions were realised with a 90° angle between the sample surface and analyser. A pass energy of 30 eV and a step size of 0.1 eV were used for Al and Ga core levels. The binding energy was calibrated with respect to the C–C bond component of the C 1s edge considered at 285.0 eV. Raman spectra of ZnO NWs on glass substrates were acquired with a HORIBA/JOBIN YVON Labram spectrometer equipped with a liquid-nitrogen-cooled CCD detector. A 488nm (514.5nm) Ar^+ laser line with a power on the surface around 7 (4) mW and an acquisition time of 600 (3600) s were used to collect the Raman spectra over the ranges of 0-800 (3000-3700) cm^{-1}, respectively. The laser was focused with a 100 x objective to obtain a ≈1µm² spot. All the Raman spectra were calibrated with a silicon reference sample considering the theoretical Raman line set to 520.7cm^{-1}. Total transmittance measurements were achieved over a wavelength range of 250-800 nm with a 1 nm step using a PERKIN ELMER Lambda 950 UV-Vis-NIR spectrophotometer equipped with an integrating sphere. The optical band gap energy was deduced from the intercept of the linear portion of $(\alpha h\upsilon)^2$ vs $h\upsilon$ graph with the $h\upsilon$-axis where α is the absorption coefficient, using the Tauc plot approach.[31]

2.3. Thermodynamic computations. Thermodynamic simulations were achieved using Visual MINTEQ software to establish the speciation diagrams of Al(III) and Ga(III) species at 85 °C for each growth condition (*i.e.*, with varying NH_3, $Al(NO_3)_3$ and $Ga(NO_3)_3$ concentrations). The two single metallic cations in aqueous solution (Al^{3+} and Ga^{3+} ions) denoted as M^{x+} are able to form hydroxide complexes with HO^- ions as the only possible ligand denoted as L, according to the general reactions: $nM^{x+} + iL \leftrightarrow M_nL_i^{nx+}$, where $M_nL_i^{nx+}$ is the complex considered, i is the coordination number, and x is the cation charge. The related stability constants β_i^L associated to each reaction are given by: $\beta_i^L = \frac{[M_nL_i^{nx+}]}{[M^{x+}]^n[L]^i}$. These constants were taken at 25 °C from NIST for Al(III) and Ga(III) species and deduced at 85 °C from Van't Hoff relation.

3. RESULTS AND DISCUSSION

3.1. Strategy for the simultaneous co-doping of ZnO nanowires. The doping by CBD stems from the adsorption process of Al(III) and Ga(III) species on the charged surfaces of ZnO NWs, which are mainly driven by electrostatic interactions when using column III-A group elements.[21-22] The adsorption process is highly dependent upon the pH and favourable for the subsequent incorporation of Al and Ga dopants into ZnO NWs. In order to establish the strategy for the simultaneous co-doping of ZnO NWs with Al and Ga, the speciation diagrams of Al(III) and Ga(III) species as a function of pH are presented in **Figure 1a** using Visual MINTEQ software. In the low pH-region, $Al(OH)_3$ and $Ga(OH)_3$ precipitates as well as their soluble counterparts are predominantly formed. In contrast, in the high pH-region, $Al(OH)_4^-$ and $Ga(OH)_4^-$ complexes constitute the dominant Al(III) and Ga(III) species, respectively. Interestingly, Zn(II), Al(III) and Ga(III) species do not interact each other to form additional complexes on the investigated range of pH. The transition from neutral to negatively charged Al(III) and Ga(III) species operates at a different pH value of about 6.9 and 8.4, respectively. By employing the widely used conditions involving $Zn(NO_3)_2$ and HMTA as the only chemical precursors, the growth of ZnO NWs by CBD takes place at a pH value of around 6,[32] which has been found to be not favourable for the incorporation of Al and Ga dopants.[21-22] In contrast, by using tailored specific conditions involving ammonia as a chemical additive, the growth of ZnO NWs proceeds at an increased pH above a value of about 8.5.[33] This stabilises Zn(II) species as $Zn(NH_3)_4^{2+}$ complexes to reduce the homogeneous growth in the bulk solution as well as Al(III) and Ga(III) species in their negatively charged complex form to perform the simultaneous co-doping. Given that the point of zero charge (PZC) value of the Zn-polar *c*- and non-polar *m*-planes is respectively of 8.7 ± 0.2 and 10.2 ± 0.2 at room temperature,[34-35] the sidewalls of ZnO NWs are positively charged in the high pH range.[19] Attractive electrostatic interactions thus drive the adsorption process of $Al(OH)_4^-$ and $Ga(OH)_4^-$ complexes, as depicted in **Figure 1b**. The *in situ* temperature and pH measurements are presented in **Figure S1** of Supporting Information. The range of experimental pH of the solution where the growth of ZnO NWs proceeds is indicated by a grey-coloured rectangular area in **Figure 1a**. The measured pH at the end of the growth of non-intentionally doped ZnO NWs points at 8.7. Interestingly, the measured pH during the growth of Al- and Ga-doped ZnO NWs slightly increases when $Al(NO_3)_3$ is added to the chemical bath, and conversely decreases slightly when $Ga(NO_3)_3$ is added to the chemical bath.

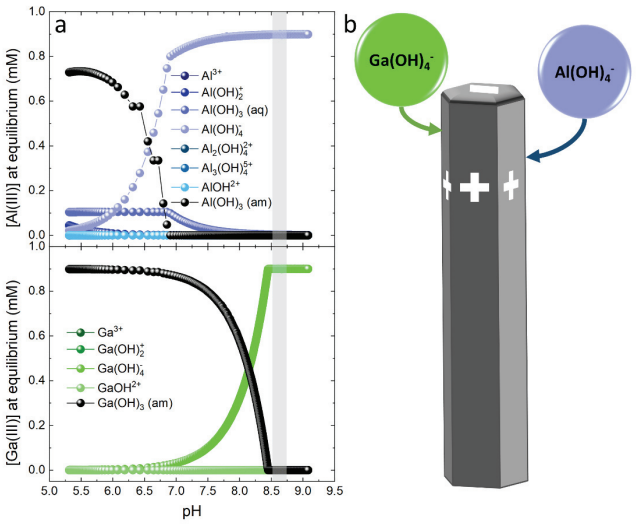

Figure 1. (a) Distribution of Al(III) and Ga(III) species at 85°C as a function of pH, as computed by Visual MINTEQ software. The NH_3 concentration was varied in the range of 0−1500 mM, while the $Al(NO_3)_3$ and $Ga(NO_3)_3$ concentrations were set to 0.9 mM. Each data point corresponds to the addition of 1 mM of NH_3 in the chemical bath. The grey rectangular area denotes the range of pH values experimentally measured at the end of the CBD process. (b) Schematic representing the adsorption processes of $Al(OH)_4^-$ and $Ga(OH)_4^-$ complexes on the charged surfaces of ZnO NWs during CBD. The sign of the surface electrical charge is taken at the pH value used during the CBD process, considering the PZC values of both the top polar *c*-planes and nonpolar *m*-plane sidewalls of ZnO NWs around 8.7 ± 0.2 and 10.2 ± 0.2 at room temperature.[34-35]

3.2. Influence of the simultaneous co-doping on the morphology of ZnO nanowires. The morphology of non-intentionally doped and Al- and Ga-doped ZnO NWs grown by CBD is presented in **Figure 2a** using FESEM imaging. Non-intentionally doped ZnO NWs and Al-doped ZnO NWs with a $[Al(NO_3)_3]/[Zn(NO_3)_2]$ ratio of 3% present a typical narrow pencil-like tip. This originates from the incomplete formation of the nonpolar *m*-planes on the sidewalls of ZnO NWs owing to their high axial growth rate. In contrast, ZnO NWs grown in the other conditions all exhibit a typical hexagonal shape characteristic of their wurtzite structure oriented along the polar *c*-axis, together with a moderate vertical alignment. The evolution of the length and diameter as a function of the $[Al(NO_3)_3]/[Zn(NO_3)_2]$ and $[Ga(NO_3)_3]/[Zn(NO_3)_2]$ ratios is presented in **Figure 2b,c**. The length of Al- and Ga-doped ZnO NWs first decreases strongly from 3923 ± 193 nm to 1761 ± 136 nm as the $[Al(NO_3)_3]/[Zn(NO_3)_2]$ ratio is increased from 0 to 2%, and then increases significantly to 3224 ± 222 nm as the $[Al(NO_3)_3]/[Zn(NO_3)_2]$ ratio is increased to 3%. The only addition of $Al(NO_3)_3$ in the chemical bath has been found to drastically decrease the length of Al-doped ZnO NWs until a $[Al(NO_3)_3]/[Zn(NO_3)_2]$ ratio of 1% and then to slightly increase their length until a $[Al(NO_3)_3]/[Zn(NO_3)_2]$ ratio of 3% prior to a more

pronounced increase as the $[Al(NO_3)_3]/[Zn(NO_3)_2]$ ratio is further increased to 10%.[36] This explains here why non-intentionally doped and Al-doped ZnO NWs roughly exhibit the same length. In contrast, the only addition of $Ga(NO_3)_3$ implies a slight reduction of the length of Ga-doped ZnO NWs until a $[Ga(NO_3)_3]/[Zn(NO_3)_2]$ ratio of 3%.[22] The present experimental data indicate that the evolution of the length of Al- and Ga-codoped ZnO NWs follows the expected behaviour when $Al(NO_3)_3$ is added to the chemical bath. Moreover, the diameter taken at half of the height of Al- and Ga-doped ZnO NWs first decreases strongly from 124 ± 28 nm to 82 ± 19 nm as the $[Al(NO_3)_3]/[Zn(NO_3)_2]$ ratio is increased from 0 to 2%, and then increases significantly to 118 ± 24 nm as the $[Al(NO_3)_3]/[Zn(NO_3)_2]$ ratio is increased to 3%. The only addition of $Al(NO_3)_3$ in the chemical bath has been shown to drastically decrease the diameter of ZnO NWs until a $[Al(NO_3)_3]/[Zn(NO_3)_2]$ ratio of 1% from which a plateau is reached.[36] In contrast, the only addition of $Ga(NO_3)_3$ implies a significant increase in the diameter of ZnO NWs until a $[Ga(NO_3)_3]/[Zn(NO_3)_2]$ ratio of 3%.[22] Again, the present experimental data reveal that the evolution of the diameter of Al- and Ga-codoped ZnO NWs follows the expected behaviour when $Al(NO_3)_3$ is added to the chemical bath. Interestingly, the aspect ratio of ZnO NWs increases as the $[Al(NO_3)_3]/[Zn(NO_3)_2]$ ratio is increased, and correlatively decreases as the $[Ga(NO_3)_3]/[Zn(NO_3)_2]$ ratio is increased as seen in **Figure 2d**. As a result, the dimensions and the shape of Al- and Ga-codoped ZnO NWs are overall driven mainly by the Al(III) species in the chemical bath. $Al(OH)_4^-$ complexes hence act predominantly on their sidewalls as compared to $Ga(OH)_4^-$ complexes that are liable to be more stable in the sub-surfaces as suggested by DFT calculations.[37]

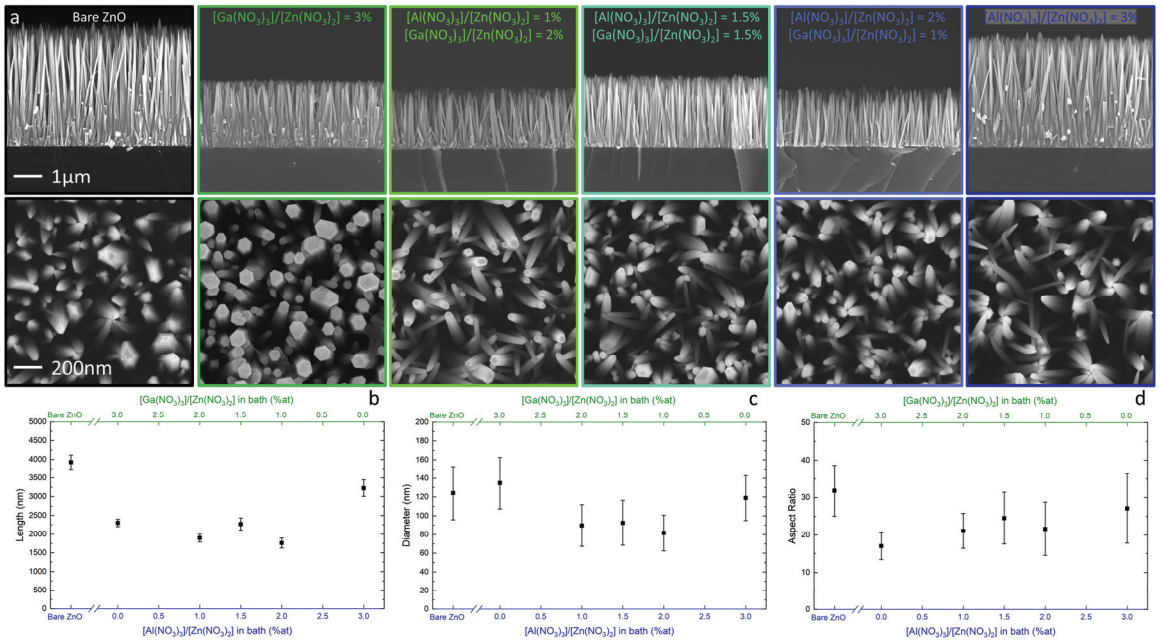

Figure 2. (a) Top-view and cross-sectional view FESEM images of non-intentionally doped, Al- and Ga-doped ZnO NWs grown by CBD. The scale bar is the same for each top-view and cross-sectional view, respectively. Evolution of the (b) length, (c) diameter, and (d) aspect ratio of non-intentionally doped, Al- and Ga-doped ZnO NWs as a function of the $[Al(NO_3)_3]/[Zn(NO_3)_2]$ and $[Ga(NO_3)_3]/[Zn(NO_3)_2]$ ratios. The diameter was measured at half of the height of ZnO NWs.

3.3. Influence of the simultaneous co-doping on the phase of ZnO nanowires. XRD patterns of non-intentionally doped, Al- and Ga-doped ZnO NWs grown by CBD before and after thermal annealing are presented in **Figure 3a-d**. The diffraction peaks pointing at 31.76, 34.42, 36.24, 47.53, 56.57, 62.85, 67.93, 69.06, 72.56 and 76.93° correspond to the wurtzite structure of ZnO NWs, indicating the formation of a pure zincite phase before and after thermal annealing as shown in **Figure 3a,c**. The dominant (0002) diffraction peak at 34.42 ° reveals that non-intentionally doped, Al- and Ga-doped ZnO NWs all grow along the polar *c*-axis. The other diffraction peaks originates from the non-intentionally doped, Al- and Ga-doped ZnO NWs that are not perfectly aligned vertically as observed by FESEM imaging in **Figure 2**. No additional diffraction peaks coming from the presence of Zn, Al or Ga precipitates in the form of oxides, hydroxides, or oxy-hydroxides phases are detected. This is well correlated with the thermodynamic simulations presented above and the fact that the growth kinetic of ZnO NWs is relatively fast as compared to that of other possible precipitates. Interestingly, a significant shift of the diffraction peaks towards the lower or higher angles occurs, depending on the (hkl) Miller indices. As an illustration, a zoom-in around the (0004) diffraction peak is

presented in **Figure 3b,d**. As the $[Ga(NO_3)_3]/[Zn(NO_3)_2]$ ratio is increased from 0 to 3%, the (0004) diffraction progressively shifts towards higher angles from 72.546 to 72.631°. In contrast, the (0004) diffraction peak keep the same value as the $[Al(NO_3)_3]/[Zn(NO_3)_2]$ ratio reaches 3%. In order to determine the *c*- and *a*-lattice parameters, the XRD patterns were refined using Celref 3 software, as presented in **Figure 3e-g**. The unit cell volume in as-grown non-intentionally doped, Al- and Ga-doped ZnO NWs keep a fairly constant value of around 47.6 $Å^3$, which is very close to the value of bulk ZnO. In contrast, the unit cell volume in annealed non-intentionally doped, Al- and Ga-doped ZnO NWs decreases from 47.5 to 47.3 $Å^3$ as the $[Ga(NO_3)_3]/[Zn(NO_3)_2]$ ratio is increased from 0 to 2%. Surprisingly, it further increases to a value of around 47.6 $Å^3$ that is close to bulk ZnO, as the $[Ga(NO_3)_3]/[Zn(NO_3)_2]$ ratio reaches 3% where no $Al(NO_3)_3$ was added to the chemical bath. More interestingly, the *c*-lattice parameter before thermal annealing continuously decreases from 5.208 to 5.203 Å as the $[Ga(NO_3)_3]/[Zn(NO_3)_2]$ ratio is increased from 0 to 3%. This indicates the progressive significant insertion of Ga dopants in the wurtzite structure of ZnO NWs, as the Ga ionic radius of 0.62 Å is smaller than the Zn ionic radius of 0.74 Å. Ga dopant is known to substitute for Zn atom (Ga_{Zn}), acting as a shallow donor, with a very low concentration of Ga_i having a much higher formation energy.[38] The *c*-lattice parameter after thermal annealing gets closer to the value of bulk ZnO, revealing a significant strain relaxation. This suggests a redistribution of Al- and Ga-related defects after thermal annealing, for instance through the formation of (Ga_{Zn}–V_{Zn}) complexes acting as compensatory acceptors.[38] In contrast, the *a*-lattice parameter before thermal annealing keeps a fairly constant value of around 3.251 Å, as the $[Ga(NO_3)_3]/[Zn(NO_3)_2]$ ratio is increased from 0 to 3%. Notably, the *a*-lattice parameter after thermal annealing decreases from 3.246 to 3.239 Å as the $[Ga(NO_3)_3]/[Zn(NO_3)_2]$ ratio is increased from 0 to 2%. It further increases to a value of around 3.251 Å that is close to bulk ZnO, as the $[Ga(NO_3)_3]/[Zn(NO_3)_2]$ ratio reaches 3% where no $Al(NO_3)_3$ was added to the chemical bath. Additionally, when the $[Al(NO_3)_3]/[Zn(NO_3)_2]$ ratio reaches 3% where no $Ga(NO_3)_3$ was added to the chemical bath, the *c*- and *a*-lattice parameters before and after thermal annealing are closer to the values of bulk ZnO and hence affected to a lesser extent. This suggests that the insertion of Al dopants in the wurtzite structure of ZnO NWs is less pronounced despite its ionic radius of 0.54 Å. Al dopant is also known to substitute for Zn atom (Al_{Zn}), acting as a shallow donor, again with a very low concentration of Al_i exhibiting a much higher formation energy.[39] In the case of the simultaneous doping with

Al and Ga, interplay effects creating additional Al- and Ga-related defects are expected, affecting more the *a*-lattice parameter than the *c*-lattice parameter as also reported in Al- and Ga-codoped ZnO thin films.[40]

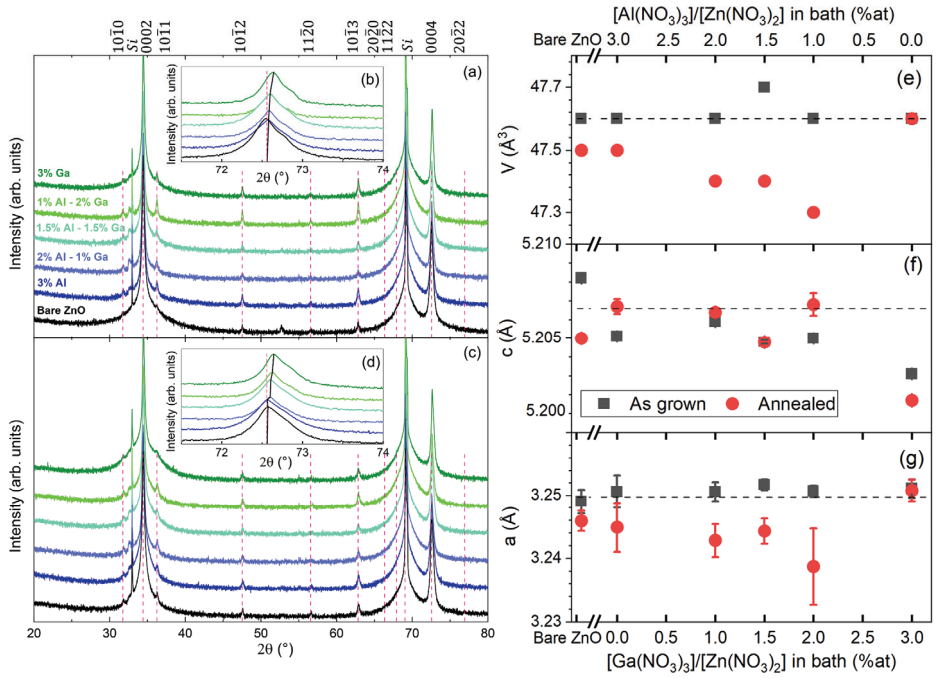

Figure 3. XRD patterns of non-intentionally doped, Al- and Ga-doped ZnO NWs grown by CBD (a,b) before and (c,d) after thermal annealing at 400 °C for 1 hour under oxygen atmosphere as a function of the $[Ga(NO_3)_3]/[Zn(NO_3)_2]$ and $[Al(NO_3)_3]/[Zn(NO_3)_2]$ ratios in the chemical bath. (e) Volume of the ZnO unit cell, (f) *c*-lattice parameter, and (g) *a*-lattice parameter as a function of the $[Ga(NO_3)_3]/[Zn(NO_3)_2]$ and $[Al(NO_3)_3]/[Zn(NO_3)_2]$ ratios in the chemical bath. The dashed lines indicate the reference values as obtained from the 00-036-1451 ICDD file.

3.4. Incorporation of Al and Ga dopants into ZnO nanowires. ICP-MS measurements of non-intentionally doped, Al-and Ga-doped ZnO NWs diluted in nitric acid solution were performed to identify metal traces and quantitatively estimate the amount of incorporated Al and Ga dopants. The ICP-MS data are defined as the atomic ratio of Al and Ga dopants over Zn to avoid the impact of the initial amount of ZnO NWs diluted in nitric acid solution. The evolution of the Ga/Zn and Al/Zn atomic ratios in non-intentionally doped, Al- and Ga-doped ZnO NWs before and after thermal annealing as a function of the $[Ga(NO_3)_3]/[Zn(NO_3)_2]$ and $[Al(NO_3)_3]/[Zn(NO_3)_2]$ ratios are presented in **Figure 4**. The mass concentration of Zn, Al and Ga dopants in nitric acid solutions along with the dilution factor used are reported in **Table S1** of Supporting Information. In non-intentionally doped ZnO NWs, the low residual Ga/Zn and Al/Zn atomic ratios of 1.3 and 10.6 ppm are detected, corresponding to the contamination of the $Zn(NO_3)_2$ and HMTA chemical precursors with residual

impurities.[33] The Ga/Zn atomic ratio in Al- and Ga-doped ZnO NWs linearly increases from 1.3 x 10^{-4} to 0.89 % as the $[Ga(NO_3)_3]/[Zn(NO_3)_2]$ ratio is increased from 0 to 3%. This reveals that one third of the initial Ga(III)/Zn(II) species ratio in the chemical bath is incorporated into Al- and Ga-doped ZnO NWs, and that the Al(III) species in the chemical bath have no effect on the amount of Ga into Al- and Ga-doped ZnO NWs. In contrast, the Al/Zn atomic ratio in Al- and Ga-doped ZnO NWs initially increases from 1.06 x 10^{-3} to 0.14 % as the $[Al(NO_3)_3]/[Zn(NO_3)_2]$ ratio is increased from 0 to 1%, but saturates to the value of 0.15 % as the $[Al(NO_3)_3]/[Zn(NO_3)_2]$ ratio is further increased to 2%. A maximum Al/Zn atomic ratio of 0.47 % in Al-doped ZnO NWs is measured when the $[Al(NO_3)_3]/[Zn(NO_3)_2]$ ratio reaches 3%. At maximum, one sixth of the initial Al(III)/Zn(II) species ratio in the chemical bath is incorporated into Al-doped ZnO NWs. This indicates that the incorporation of Al dopants into Al- and Ga-codoped ZnO NWs is affected by the Ga(III) species in the chemical bath, and limited to a value of about 0.15 %. The amount of incorporated Ga dopants into ZnO NWs is therefore much larger than the amount of incorporated Al dopants when a single doping strategy is used, but also when a co-doping strategy is employed. Additionally, the amount of Al and Ga dopants into ZnO NWs is not affected by the thermal annealing at 400 °C for 1 hour under oxygen atmosphere, such that the Ga/Zn and Al/Zn atomic ratios keep the same values.

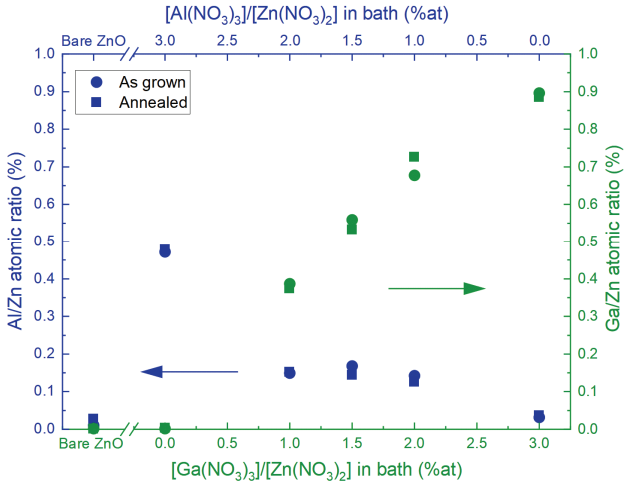

Figure 4. Evolution of the Ga/Zn and Al/Zn atomic ratios in non-intentionally doped, Al- and Ga-doped ZnO NWs before and after thermal annealing at 400 °C for 1 hour under oxygen atmosphere as a function of the $[Ga(NO_3)_3]/[Zn(NO_3)_2]$ and $[Al(NO_3)_3]/[Zn(NO_3)_2]$ ratios in the chemical bath as obtained from ICP-MS measurements.

A bright-field TEM image and a typical STEM-EDS spectrum of a single Al- and Ga-codoped ZnO NW grown with $[Al(NO_3)_3]/[Zn(NO_3)_2]$ and $[Ga(NO_3)_3]/[Zn(NO_3)_2]$ ratios of 1.5% in the chemical bath are presented in **Figure 5a,b**. The TEM analysis reveals that no extended defects are formed following the incorporation of Al and Ga dopants into ZnO NWs. In the low energy range, the Zn L_α line occurs at 1.01 keV along with the Al K_α line being detected at 1.486 keV. In the high energy range, the Zn K_α and K_β lines occur at 8.63 and 9.57 keV, respectively, together with the Ga K_α and K_β lines being detected at 9.25 and 10.26 keV, respectively. A quantitative analysis of the STEM-EDS spectra yields an Al atomic ratio of around 0.19 % and a Ga atomic ratio of around 0.59 %, confirming that the amount of Ga dopants incorporated into ZnO NWs is roughly three times larger than the amount of incorporated Al dopants as measured by ICP-MS. This emphasizes the relevance of ICP-MS measurements to quantitatively assess the incorporation of dopants into ZnO NWs. The corresponding STEM-EDS elemental maps are presented in **Figure 5c**, showing that the spatial distribution of Al and Ga dopants in ZnO NWs is homogeneous.

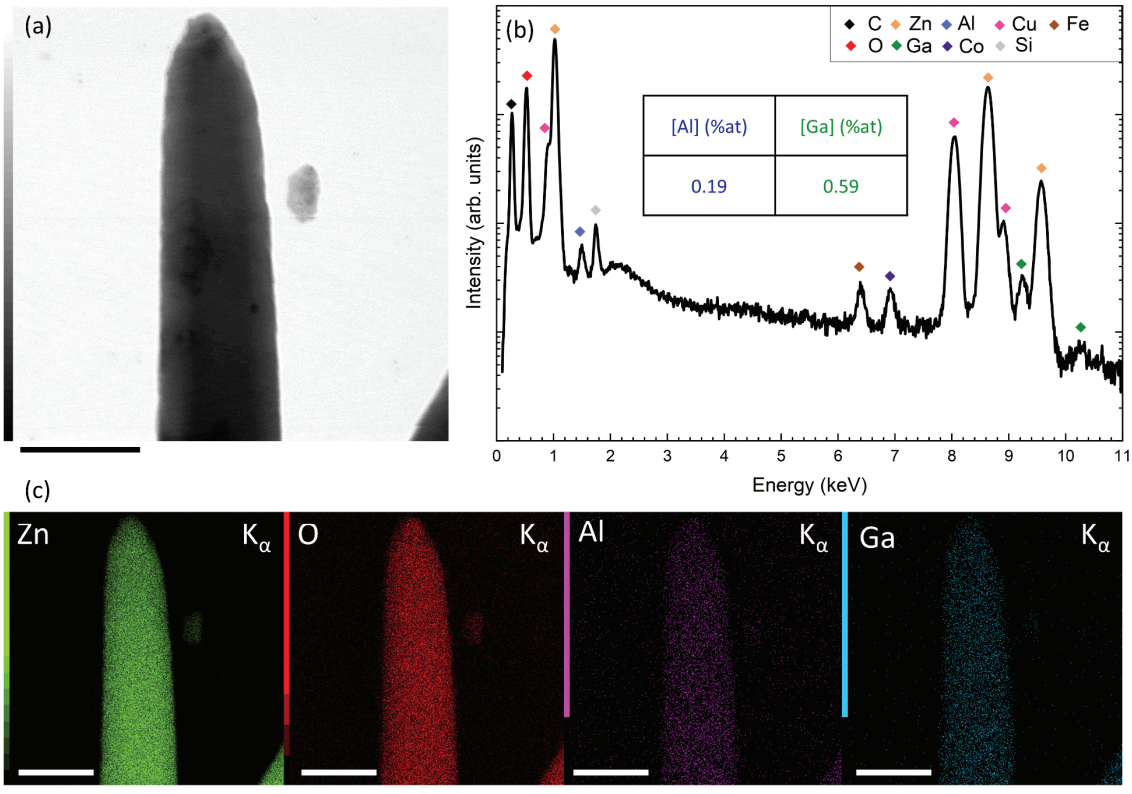

Figure 5. (a) Bright-field TEM image collected on a single Al- and Ga-codoped ZnO NW grown with $[Al(NO_3)_3]/[Zn(NO_3)_2]$ and $[Ga(NO_3)_3]/[Zn(NO_3)_2]$ ratios of 1.5% in the chemical bath. (b) Corresponding typical STEM-EDS spectrum. The C, Cu and Si signals come from the holder, grid, and substrate, respectively,

while the Co and Fe signals originate from the TEM column. (c) Corresponding STEM-EDS elemental maps of the Zn (green), O (red), Al (pink) and Ga (blue) elements. The scale bar is 100 nm.

XPS measurements of non-intentionally doped, Al- and Ga-doped ZnO NWs were performed to assess their surface composition. XPS spectra of the Ga 3d core level are presented in **Figure 6a**. The Ga-related peak at around 20 eV is detected in Ga-doped ZnO NWs when $Ga(NO_3)_3$ was added to the chemical bath and corresponds to Ga^{3+} ions.[41] As expected, it is not observed in non-intentionally doped and Al-doped ZnO NWs. The peaks at 19 and 22 eV are attributed to the Zn 3d and O 2s core levels, respectively. Before thermal annealing, the relative intensity of the Ga-related peak increases as the $[Ga(NO_3)_3]/[Zn(NO_3)_2]$ ratio is increased from 0 to 1%, and then saturates to a constant value as the $[Ga(NO_3)_3]/[Zn(NO_3)_2]$ ratio is further increased to 3%. The surface of Al- and Ga-codoped ZnO NWs thus seems to be saturated with Ga from the $[Ga(NO_3)_3]/[Zn(NO_3)_2]$ ratio of 1.5%. After thermal annealing, the relative intensity of the Ga-related peak in Al- and Ga-codoped ZnO NWs decreases, indicating that a smaller amount of Ga is located on the surface. In contrast, the intensity of the Ga-related peak in Ga-doped ZnO NWs when no $Al(NO_3)_3$ was added increases, revealing an enrichment of the surface with Ga. XPS spectra of the Al 2p core level are presented in **Figure 6b**. The Al-related peak at around 74 eV is only detected in Al-doped ZnO NWs when the $[Al(NO_3)_3]/[Zn(NO_3)_2]$ ratio reaches 3% and corresponds to Al^{3+} ions.[42] After thermal annealing, the relative intensity of the Al-related peak significantly decreases, also indicating that a smaller amount of Al is located on the surface. The XPS measurement is here hindered by its detection limit of around 0.5%, which is close to the Al/Zn atomic ratio measured by ICP-MS. This should be taken into account for the absence of the Al-related peak in Al- and Ga-codoped ZnO NWs for which the Al content is under the detection limit.

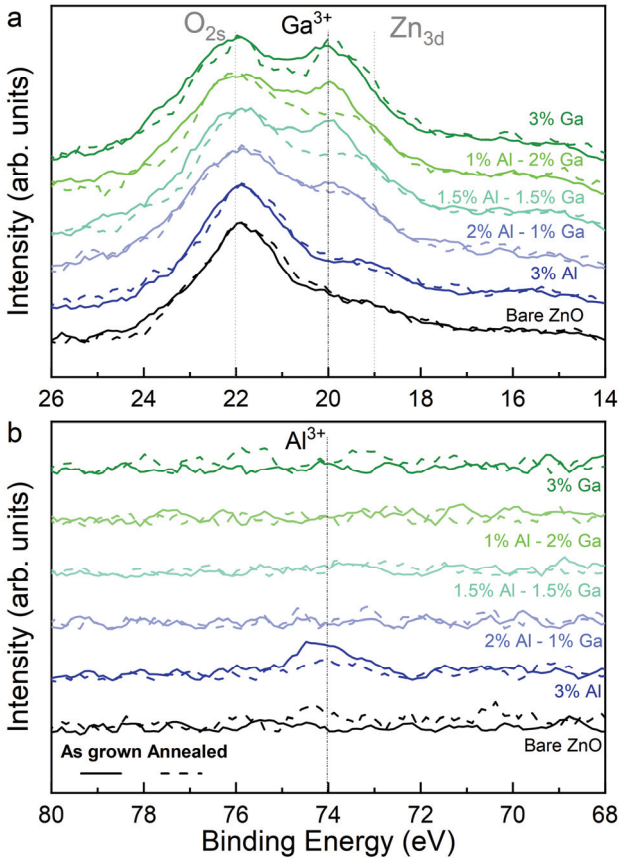

Figure 6. (a) XPS spectra of the Ga 3d core level of non-intentionally doped, Al- and Ga-doped ZnO NWs before (solid lines) and after (dashed lines) thermal annealing at 400 °C for 1 hour under oxygen atmosphere as a function of the $[Ga(NO_3)_3]/[Zn(NO_3)_2]$ and $[Al(NO_3)_3]/[Zn(NO_3)_2]$ ratios in the chemical bath. (b) XPS spectra of the Al 2p core level of non-intentionally doped, Al- and Ga-doped ZnO NWs before (solid lines) and after (dashed lines) thermal annealing at 400 °C for 1 hour under oxygen atmosphere as a function of the $[Ga(NO_3)_3]/[Zn(NO_3)_2]$ and $[Al(NO_3)_3]/[Zn(NO_3)_2]$ ratios in the chemical bath.

The Raman spectra of non-intentionally doped, Al- and Ga-doped ZnO NWs before and after thermal annealing are presented in **Figures 7** and **8**. In the low wavenumber range from 50 to 800 cm^{-1} as seen in **Figure 7a,b**, the phonon modes characteristic of the wurtzite structure of ZnO NWs before and thermal annealing point at 101 (E_2^{Low}), 332 (E_2^{High}- E_2^{Low}), 437 (E_2^{High}), and 574 cm^{-1} (A_1(LO)), respectively.[43] Other Raman lines from the wurtzite structure do not occur owing to the relative vertical alignment of ZnO NWs along the polar *c*-axis. Interestingly, the position of the E_2^{High} line shifts from 438.1 to 440.4 cm^{-1} before thermal annealing as the $[Ga(NO_3)_3]/[Zn(NO_3)_2]$ ratio is increased from 0 to 3%, as shown in **Figure S2** of Supporting Information. In contrast, the position of the E_2^{High} line after thermal annealing is almost constant around the value of 437.4 cm^{-1}. Both of them are well correlated with the evolution of the *c*- and *a*-lattice parameters

deduced from XRD measurements. Moreover, two additional modes located at 631 cm^{-1} (AM_{Ga1}) and 696 cm^{-1} (AM_{Ga2}) are attributed to the incorporation of Ga dopants[22, 44] and are observed before and after thermal annealing exclusively when $Ga(NO_3)_3$ was added to the chemical bath. The AM_{Ga1}/E_2^{High} and AM_{Ga2}/E_2^{High} intensity ratios continuously increase before and after thermal annealing as the $[Ga(NO_3)_3]/[Zn(NO_3)_2]$ ratio is increased from 0 to 3%, as shown in **Figure 7c,d**. This indicates the gradual incorporation of Ga dopants into Al- and Ga-codoped ZnO NWs as the $[Ga(NO_3)_3]/[Zn(NO_3)_2]$ ratio is increased. Notably, the AM_{Ga1}/E_2^{High} and AM_{Ga2}/E_2^{High} intensity ratios are significantly higher before thermal annealing for a given $[Ga(NO_3)_3]/[Zn(NO_3)_2]$ ratio. This may indicate again the redistribution of Ga-related defects after thermal annealing. Importantly, standard additional modes pointing at 276 (AM_1), 509 (AM_2), 579 (AM_3), 623 (AM_4), and 643 cm^{-1} (AM_5)[21-22, 44] occur in non-intentionally-doped, Al- and Ga-doped ZnO NWs mainly after thermal annealing, as seen in **Figure 7b**. They are assigned to the B_1^{Low}, $2B_1^{Low}$, B_1^{High}, $TA+B_1^{High}$, and $B_1^{Low}+B_1^{High}$ silent modes, respectively, which originates from disordered-activated Raman scattering due to the breakdown of the translational symmetry of the crystal lattice.[45] The presence of these AM modes with a low intensity in non-intentionally doped ZnO NWs was discussed in Ref.[33] and comes from the incorporation of residual nitrogen from HMTA and NH_3 molecules and/or from residual metallic impurities involving Al and Ga in the chemical precursors as quantified by ICP-MS measurements above. These AM modes also exhibit a lower intensity in Al-doped ZnO NWs, indicating the smaller amount of Al dopants. Importantly, the AM/E_2^{High}

intensity ratio significantly increases as the $[Ga(NO_3)_3]/[Zn(NO_3)_2]$ ratio is increased from 0 to 3%, again revealing the gradual incorporation of Ga dopants into Al- and Ga-codoped ZnO NWs.

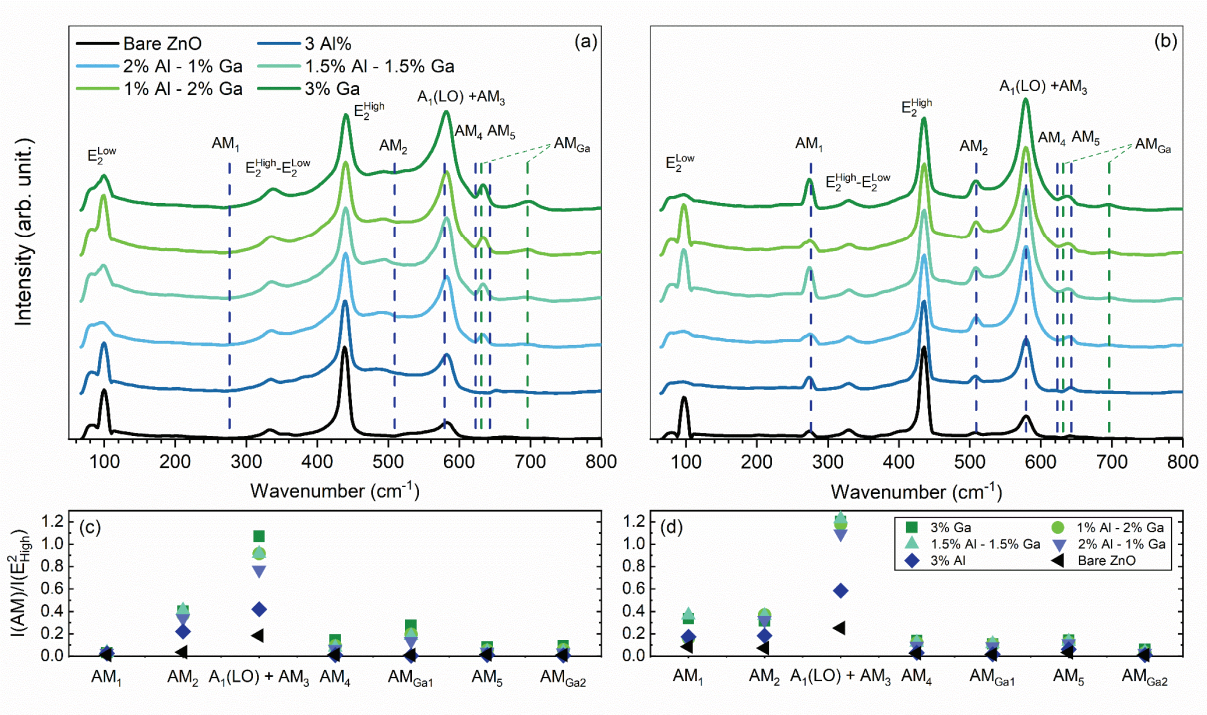

Figure 6. Raman spectra in the low wavenumber range for non-intentionally doped, Al- and Ga-doped ZnO NWs (a) before and (b) after thermal annealing at 400 °C for 1 hour under oxygen atmosphere as a function of the $[Ga(NO_3)_3]/[Zn(NO_3)_2]$ and $[Al(NO_3)_3]/[Zn(NO_3)_2]$ ratios in the chemical bath. (c,d) Intensity ratio of the AM over E_2^{High} lines of non-intentionally doped, Al- and Ga-doped ZnO NWs (c) before and (d) after thermal annealing at 400 °C for 1 hour under oxygen atmosphere as a function of the $[Ga(NO_3)_3]/[Zn(NO_3)_2]$ and $[Al(NO_3)_3]/[Zn(NO_3)_2]$ ratios in the chemical bath.

In the high wavenumber range from 3000 to 3700 cm^{-1} as seen in **Figure 8a,b**, a couple of sharp Raman lines and broad Raman bands are attributed to the incorporation of hydrogen- and nitrogen-related defects into ZnO NWs.[20] Before thermal annealing as presented in **Figure 8a**, an asymmetric Raman band centred at 3575 cm^{-1} is dominated by a Raman line assigned to interstitial hydrogen in the bond-centred site (H_{BC})[46] and exhibits a shoulder around 3500 cm^{-1} ascribed to O−H bonds[47] on the surface of ZnO NWs. The intensity of the H_{BC} line is slightly reduced when $Al(NO_3)_3$ was added to the chemical bath, regardless of the $[Al(NO_3)_3]/[Zn(NO_3)_2]$ and $[Ga(NO_3)_3]/[Zn(NO_3)_2]$ ratios. The incorporation of Al dopants thus affects somehow the formation of H_{BC}. In contrast, the intensity of the H_{BC} line significantly increases when only $Ga(NO_3)_3$ was added to the chemical bath, along with the shoulder attributed to the O−H bonds that is more

pronounced. Another asymmetric broad Raman band centred around 3375 cm^{-1} is assigned to (V_{Zn}-nH) defect complexes,[20] involving several contributions from V_{Zn}-H,[46] V_{Zn}-2H,[46] and V_{Zn}-3H[48] defect complexes in the wavenumber range of 3300-3418 cm^{-1}. Interestingly, the intensity of the V_{Zn}-nH band is much lower in Al- and Ga-doped ZnO NWs as compared to non-intentionally doped ZnO NWs. This indicates that the formation of V_{Zn}-nH defect complexes is hampered by the incorporation of Al and Ga dopants into ZnO NWs. After thermal annealing as presented in **Figure 8b**, the H_{BC} and O−H bond related lines along with the V_{Zn}-nH related line vanish as expected from Ref.[49] when a temperature of 400 °C is used. However, the vanishing of the H_{BC} line is less marked in Al-doped ZnO NWs.

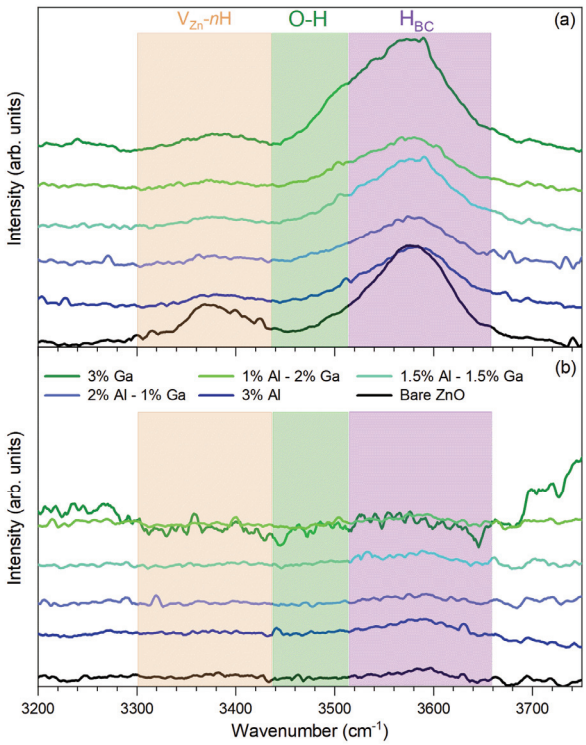

Figure 7. Raman spectra in the low wavenumber range for non-intentionally doped, Al- and Ga-doped ZnO NWs (a) before and (b) after thermal annealing at 400 °C for 1 hour under oxygen atmosphere as a function of the $[Ga(NO_3)_3]/[Zn(NO_3)_2]$ and $[Al(NO_3)_3]/[Zn(NO_3)_2]$ ratios in the chemical bath.

The Tauc plots of non-intentionally doped, Al- and Ga-doped ZnO NWs before and after thermal annealing are presented in **Figure 9**. Before thermal annealing, the optical band gap energy in Al-doped ZnO NWs is found to increase from 3.24 to 3.30 eV as the $[Al(NO_3)_3]/[Zn(NO_3)_2]$ ratio is increased from 0 to 3%. This increase was also reported in Al-doped ZnO thin films[50] and typically originates from the Burstein-Moss shift,[51-52] where the Fermi level exceeds the bottom of the conduction band owing to a free electron density

above the critical concentration of 4.2 x 10^{18} cm^{-3}.[53] In contrast, the optical band gap energy in Ga-doped ZnO NWs decreases from 3.24 to 3.23 eV as the $[Ga(NO_3)_3]/[Zn(NO_3)_2]$ ratio is increased from 0 to 3%. This comes from the band gap renormalization stemming from the hybridization of Ga-related orbitals with the orbitals composing the bottom of the conduction band.[54] In addition to the Burstein-Moss phenomenon and band gap renormalization process, the strain induced by the incorporated Al and Ga dopants may also play a significant role on the optical band gap energy. The variation of the optical band gap energy in Al- and Ga-codoped ZnO NWs is overall driven by the dominant dopants depending on the $[Al(NO_3)_3]/[Zn(NO_3)_2]$ and $[Ga(NO_3)_3]/[Zn(NO_3)_2]$ ratios. After thermal annealing, the optical band gap energy keeps a rather constant value around 3.26 eV (except for Ga-doped ZnO NWs), which is likely due to the significant strain relaxation as reported by XRD and Raman scattering measurements.

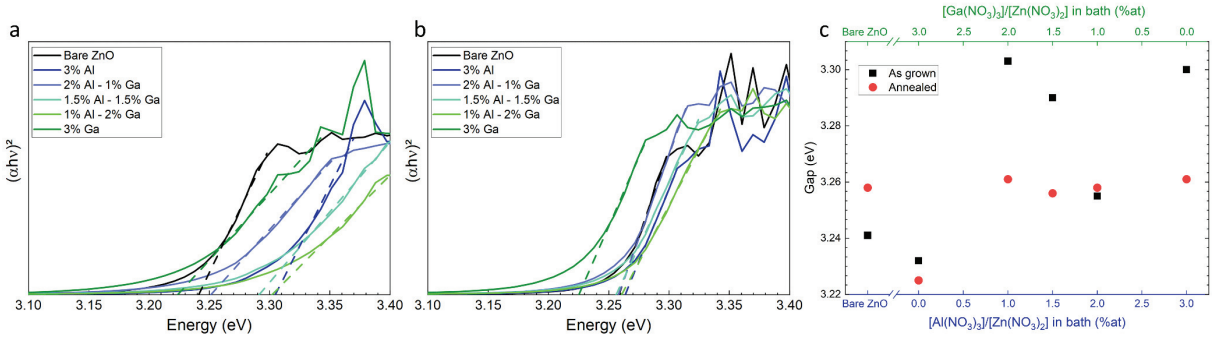

Figure 9. Tauc plots in non-intentionally doped, Al- and Ga-doped ZnO NWs (a) before and (b) after thermal annealing at 400 °C for 1 hour under oxygen atmosphere as a function of the $[Ga(NO_3)_3]/[Zn(NO_3)_2]$ and $[Al(NO_3)_3]/[Zn(NO_3)_2]$ ratios in the chemical bath. The dashed lines denote the fit of the linear portion to deduce the optical band gap energy from its intercept with the hυ-axis. (c) Evolution of the optical band gap energy of non-intentionally doped, Al- and Ga-doped ZnO NWs before and after thermal annealing at 400 °C for 1 hour under oxygen atmosphere as a function of the $[Al(NO_3)_3]/[Zn(NO_3)_2]$ and $[Ga(NO_3)_3]/[Zn(NO_3)_2]$ ratios in the chemical bath.

3.5. Al and Ga co-doping processes in ZnO nanowires. By using the experimental data deduced from the different characterization techniques, a schematic diagram is presented in **Figure 10** to illustrate the co-doping processes in ZnO NWs grown by CBD. First, the simultaneous co-doping of ZnO NWs with Al and Ga is shown in the high pH-region, where the adsorption process of $Al(OH)_4^-$ and $Ga(OH)_4^-$ complexes on the positively charged *m*-plane sidewalls are driven by attractive electrostatic forces, as presented in **Figure 10a**. In that sense, the chemical behaviour of Al(III) and Ga(III) species in aqueous solution is compatible, offering

a narrow range of CBD conditions where the simultaneous co-doping efficiently operates. Before thermal annealing as presented in **Figure 10b**, the incorporation of Ga dopants into ZnO NWs is larger than the incorporation of Al dopants. One third of the initial Ga(III)/Zn(II) species ratio in aqueous solution is incorporated into ZnO NWs, regardless of the $[Al(NO_3)_3]/[Zn(NO_3)_2]$ and $[Ga(NO_3)_3]/[Zn(NO_3)_2]$ ratios. In contrast, only one sixth of the initial Al(III)/Zn(II) species ratio in aqueous solution at maximum is incorporated into ZnO NWs when only $Al(NO_3)_3$ was added to the chemical bath. This is well supported by DFT calculations investigating the Ga and Al doping of ZnO.[38-39] The formation energy of Ga_{Zn} has been found to be lower than the formation energy of Al_{Zn} in the wurtzite structure of ZnO, regardless of the Fermi level and oxygen chemical potential.[55] Similarly, the Madelung energy contributing to the cohesive energy of ZnO is decreased to a larger extent by incorporating Ga_{Zn} rather than Al_{Zn}.[56] Interestingly, the incorporation of Al dopants is even smaller when $Ga(NO_3)_3$ was further added to the chemical bath. Since Ga_{Zn} preferentially forms at the expense of Al_{Zn},[55] the remaining Al dopants may be incorporated as Al_i but with a very low concentration as their formation energy is high.[39, 57] The presence of Al on the surfaces of Al- and Ga-codoped ZnO NWs is also expected significantly. This explains the fact that the morphology of Al- and Ga-codoped ZnO NWs is mainly governed by the Al(III) species acting as capping agents on the non-polar *m*-plane sidewalls. In contrast, the presence of Ga on the surfaces of Al- and Ga-codoped ZnO NWs is expected to be less pronounced and likely proceeds on the sub-surface of the non-polar *m*-plane sidewalls.[37] Interestingly, the incorporation of Al and Ga dopants into ZnO NWs also affects the incorporation of hydrogen-related defects. It first annihilates the formation of V_{Zn}-*n*H defect complexes, for which their concentration is drastically reduced and close to zero. The preferential formation of Ga_{Zn} and Al_{Zn} following the co-doping therefore proceeds at the expense of V_{Zn}-*n*H defect complexes. Second, the enhanced formation of H_{BC} when only $Ga(NO_3)_3$ was added to the chemical bath may be due to the stronger distortion of the *c*-lattice parameter favouring the incorporation of interstitial hydrogen in the wurtzite structure. In contrast, the hampered formation of H_{BC} when $Al(NO_3)_3$ was added to the chemical bath suggests that Al_i may form even with a very low concentration and somehow affects the incorporation of interstitial hydrogen. After thermal annealing as presented in **Figure 10c**, the amount of Al and Ga dopants incorporated into ZnO NWs is similar, but a redistribution of the related-defects arises along with a possible change of their location. The surfaces of Ga-doped ZnO NWs when no $Al(NO_3)_3$ was added to the chemical bath undergo an enrichment with Ga, revealing

a migration process of Ga dopants from the bulk. However, when $Al(NO_3)_3$ was added to the chemical bath, the surfaces of Al- and Ga-codoped ZnO NWs exhibit a smaller amount of Al and Ga, suggesting a migration process of Al and Ga dopants towards the bulk for instance through a V_{Zn}-assisted mechanism.[57] This is concomitant with the occurrence of standard AMs in the Raman scattering spectra, suggesting the activation of the Al doping of ZnO NWs.[21, 36] The significant presence of Al on the surfaces of ZnO NWs thus affects directly the nature and location of Ga dopants. The formation of H_{BC} is further annihilated largely at the annealing temperature of 400 °C as expected from Ref.[49]. The combination of V_{Zn}, Al_{Zn}, Ga_{Zn} and interstitial hydrogen in multi-species defect complexes is eventually not excluded as the passivation of Al_{Zn}-V_{Zn} and Ga_{Zn}-V_{Zn} defect complexes with interstitial hydrogen was found to be energetically favorable.[55] These findings show that the simultaneous co-doping of ZnO NWs with Al and Ga is feasible provided that the CBD conditions are carefully designed. The interplay effects between the different dopants including Al, Ga, and H also open some perspectives to further tune the physical properties of ZnO NWs grown by CBD.

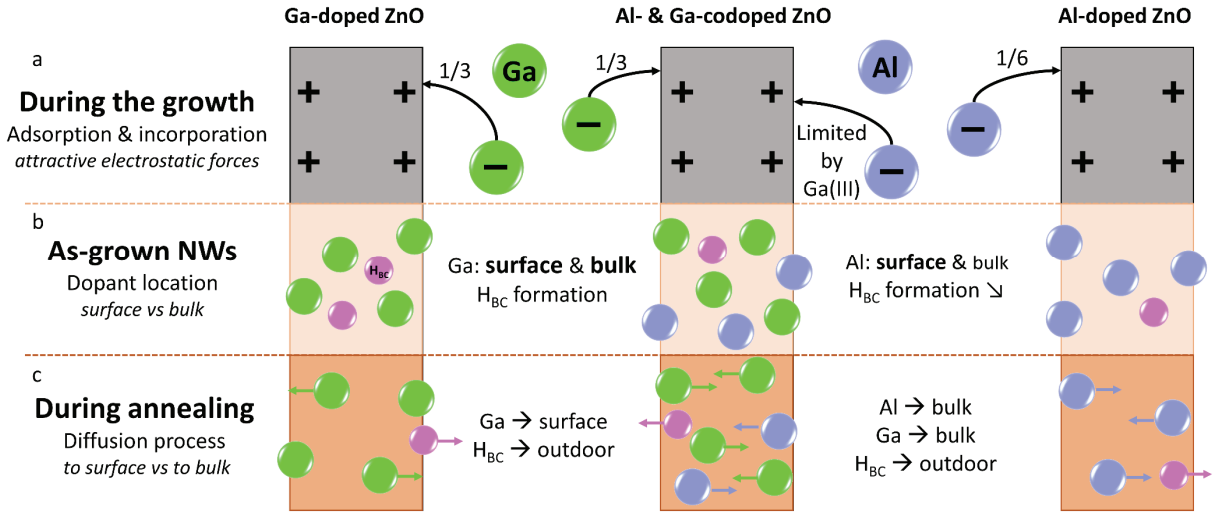

Figure 10. Schematic illustration of (a) the physicochemical processes at work in the chemical bath and of the Al and Ga co-doping processes of ZnO NWs grown by CBD (b) before and (c) after thermal annealing at 400 °C for 1 hour under oxygen atmosphere.

CONCLUSIONS

The effects of the simultaneous addition of $Al(NO_3)_3$ and $Ga(NO_3)_3$ to the chemical bath in the high pH-region on the morphology and structural properties of ZnO NWs grown by CBD as well as on the Al and Ga incorporation mechanisms have been investigated in detail. The preferential formation of $Al(OH)_4^-$ and $Ga(OH)_4^-$ complexes and the absence of interactions between the different metallic cations is shown by

thermodynamic computations. Although both $Al(OH)_4^-$ and $Ga(OH)_4^-$ complexes act as capping agents on the non-polar *m*-plane sidewalls of ZnO NWs, the structural morphology and properties are mainly governed by the effect of Al(III) species. The chemical composition of ZnO NWs as assessed by ICP-MS measurements reveals that the amount of incorporated Ga dopants linearly increases with the $[Ga(NO_3)_3]/[Zn(NO_3)_2]$ ratio up to a value of around 0.89% and hence is not affected by the Al(III) species. In contrast, the amount of incorporated Al dopants into ZnO NWs initially increases with the $[Al(NO_3)_3]/[Zn(NO_3)_2]$ ratio and then saturates to a value of around 0.15%, indicating the influence by the Ga(III) species. The amount of incorporated Ga dopants into ZnO NWs is therefore larger than the amount of incorporated Al dopants owing to energetic considerations The incorporation of Al and Ga dopants is further confirmed by XRD and Raman spectroscopy, showing the only formation of the wurtzite structure of ZnO NWs, the significant shift of the (0004) diffraction peaks and E_2^{High} phonon modes, the occurrence of AM_{Ga} at 631 and 696 cm^{-1} before and after thermal annealing and of standard AMs at 276, 509, 579, 623 and 643 cm^{-1} only after thermal annealing. The optical band gap energy is also dependent upon the content of Al and Ga in ZnO NWs as shown by UV-Vis-NIR absorption measurements. The incorporation of hydrogen-related defects is further affected by the Al and Ga dopants, notably the formation of V_{Zn}-*n*H defect complexes is annihilated. The incorporation processes of Al and Ga dopants are characterized by significant interplay effects. The Al and Ga dopants are located in the bulk of ZnO NWs but a part of Al and Ga occurs and on their surfaces, their incorporation process in the bulk being enhanced by thermal annealing under oxygen atmosphere. These findings present an efficient strategy to simultaneously achieve the co-doping of ZnO NWs grown by CBD using additional chemical precursors made of metal nitrate and to induce significant interplay effects, opening perspectives aiming at more finely tuning their optical and electrical properties for nanoscale engineering devices.

CONFLICTS OF INTEREST

There are no conflicts to declare.

ASSOCIATED CONTENT

In situ measurements of the pH and temperature during the CBD of non-intentionally doped, Al- and Ga-doped ZnO NWs (Figure S1); evolution of the E_2^{High} wavenumber position in non-intentionally doped, Al- and Ga-doped ZnO NWs before and after thermal annealing at 400 °C for 1 hour under oxygen atmosphere as a

function of the $[Al(NO_3)_3]/[Zn(NO_3)_2]$ and $[Ga(NO_3)_3]/[Zn(NO_3)_2]$ ratios in the chemical bath (Figure S2); concentration and dilution factor from ICP-MS measurements in non-intentionally doped, Al- and Ga-doped ZnO NWs before and after thermal annealing at 400 °C for 1 hour under oxygen atmosphere (Table S1).

ACKNOWLEDGMENTS

The authors acknowledge the financial support from the French Research National Agency through the DOSETTE (ANR-17-CE24-0003) and IMINEN (ANR-22-CE09-0032) projects. This work has further benefited from some of the characterization equipments of Grenoble INP-CMTC platform and of IUT 1 Chemical Department platform. It has partially been supported by the French Research National Agency in the framework of the "Investissement d'Avenir" program (ANR-15-IDEX-02) through the project CDP ECO-SESA.

NOTES AND REFERENCES

1. Schmidt-Mende, L.; MacManus-Driscoll, J. L. ZnO - Nanostructures, Defects, and Devices. *Mater. Today* **2007**, *10*, 40-48.
2. Djurišić, A. B.; Chen, X.; Leung, Y. H.; Man Ching Ng, A. ZnO Nanostructures: Growth, Properties and Applications. *J. Mater. Chem.* **2012**, *22*, 6526-6535.
3. Ozgur, U.; Alivov, Y. I.; Liu, C.; Teke, A.; Reshchikov, M. A.; Dogan, S.; Avrutin, V.; Cho, S. J.; Morkoc, H. A Comprehensive Review of ZnO Materials and Devices. *J. Appl. Phys.* **2005**, *98*, 041301.
4. Faiz, R. Zinc Oxide Light-Emitting Diodes: A Review. *Opt. Eng.* **2019**, *58*, 010901.
5. Vanmaekelbergh, D.; van Vugt, L. K. ZnO Nanowire Lasers. *Nanoscale* **2011**, *3*, 2783-2800.
6. Ouyang, W.; Chen, J.; Shi, Z.; Fang, X. Self-Powered UV Photodetectors Based on ZnO Nanomaterials. *Appl. Phys. Rev.* **2021**, *8*, 031315.
7. Consonni, V.; Briscoe, J.; Karber, E.; Li, X.; Cossuet, T. ZnO Nanowires for Solar Cells: A Comprehensive Review. *Nanotechnol.* **2019**, *30*, 362001.
8. Briscoe, J.; Dunn, S. Piezoelectric Nanogenerators - A Review of Nanostructured Piezoelectric Energy Harvesters. *Nano Energy* **2015**, *14*, 15-29.
9. Liu, J.; Wang, Y.; Ma, J.; Peng, Y.; Wang, A. A Review on Bidirectional Analogies between the Photocatalysis and Antibacterial Properties of ZnO. *J. Alloy Compd.* **2019**, *783*, 898-918.
10. Mirzaei, A.; Lee, J.-H.; Majhi, S. M.; Weber, M.; Bechelany, M.; Kim, H. W.; Kim, S. S. Resistive Gas Sensors Based on Metal-Oxide Nanowires. *J. Appl. Phys.* **2019**, *126*, 241102.
11. Kang, Y.; Yu, F.; Zhang, L.; Wang, W.; Chen, L.; Li, Y. Review of ZnO-Based Nanomaterials in Gas Sensors. *Solid State Ion.* **2021**, *360*, 115544.
12. Rackauskas, S.; Barbero, N.; Barolo, C.; Viscardi, G. ZnO Nanowire Application in Chemoresistive Sensing: A Review. *Nanomaterials* **2017**, *7*, 381.
13. Theerthagiri, J.; Salla, S.; Senthil, R. A.; Nithyadharseni, P.; Madankumar, A.; Arunachalam, P.; Maiyalagan, T.; Kim, H.-S. A Review on ZnO Nanostructured Materials: Energy, Environmental and Biological Applications. *Nanotechnol.* **2019**, *30*, 392001.
14. Xu, S.; Wang, Z. L. One-Dimensional ZnO Nanostructures: Solution Growth and Functional Properties. *Nano Res.* **2011**, *4*, 1013-1098.
15. Anastas, P.; Eghbali, N. Green Chemistry: Principles and Practice. *Chem. Soc. Rev.* **2010**, *39*, 301-312.

16. Vayssieres, L.; Keis, K.; Lindquist, S. E.; Hagfeldt, A. Purpose-Built Anisotropic Metal Oxide Material: 3D Highly Oriented Microrod Array of ZnO. *J. Phys. Chem. B* **2001**, *105*, 3350-3352.
17. McCluskey, M. D.; Jokela, S. J. Defects in ZnO. *J. Appl. Phys.* **2009**, *106*, 071101.
18. Ellmer, K.; Bikowski, A. Intrinsic and Extrinsic Doping of ZnO and ZnO Alloys. *J. Phys. D: Appl. Phys.* **2016**, *49*, 413002.
19. Joo, J.; Chow, B. Y.; Prakash, M.; Boyden, E. S.; Jacobson, J. M. Face-Selective Electrostatic Control of Hydrothermal Zinc Oxide Nanowire Synthesis. *Nat. Mater.* **2011**, *10*, 596-601.
20. Villafuerte, J.; Donatini, F.; Kioseoglou, J.; Sarigiannidou, E.; Chaix-Pluchery, O.; Pernot, J.; Consonni, V. Zinc Vacancy–Hydrogen Complexes as Major Defects in ZnO Nanowires Grown by Chemical Bath Deposition. *J. Phys. Chem. C* **2020**, *124*, 16652-16662.
21. Verrier, C.; Appert, E.; Chaix-Pluchery, O.; Rapenne, L.; Rafhay, Q.; Kaminski-Cachopo, A.; Consonni, V. Effects of the pH on the Formation and Doping Mechanisms of ZnO Nanowires Using Aluminum Nitrate and Ammonia. *Inorg. Chem.* **2017**, *56*, 13111-13122.
22. Gaffuri, P.; Appert, E.; Chaix-Pluchery, O.; Rapenne, L.; Salaun, M.; Consonni, V. The Path of Gallium from Chemical Bath into ZnO Nanowires: Mechanisms of Formation and Incorporation. *Inorg. Chem.* **2019**, *58*, 10269-10279.
23. Lausecker, C.; Salem, B.; Baillin, X.; Chaix-Pluchery, O.; Roussel, H.; Labau, S.; Pelissier, B.; Appert, E.; Consonni, V. Chemical Bath Deposition of ZnO Nanowires Using Copper Nitrate as an Additive for Compensating Doping. *Inorg. Chem.* **2021**, *60*, 1612-1623.
24. Synhaivskyi, O.; Albertini, D.; Gaffuri, P.; Chauveau, J.-M.; Consonni, V.; Gautier, B.; Bremond, G. Evidence of Piezoelectric Potential and Screening Effect in Single Highly Doped ZnO:Ga and ZnO:Al Nanowires by Advanced Scanning Probe Microscopy. *J. Phys. Chem. C* **2021**, *125*, 15373-15383.
25. Ebrahimifard, R.; Golobostanfard, M. R.; Abdizadeh, H. Sol–Gel Derived Al and Ga Co-Doped ZnO Thin Films: An Optoelectronic Study. *Appl. Surf. Sci.* **2014**, *290*, 252-259.
26. Sahoo, S. K.; Gupta, C. A.; Singh, U. P. Impact of Al and Ga Co-Doping with Different Proportion in ZnO Thin Film by Dc Magnetron Sputtering. *J. Mater. Sci.: Mater. in Electron.* **2016**, *27*, 7161-7166.
27. Makuku, O.; Mbaiwa, F.; Sathiaraj, T. S. Structural, Optical and Electrical Properties of Low Temperature Grown Undoped and (Al, Ga) Co-Doped ZnO Thin Films by Spray Pyrolysis. *Ceram. Int.* **2016**, *42*, 14581-14586.
28. Lung, C.; Toma, M.; Pop, M.; Marconi, D.; Pop, A. Characterization of the Structural and Optical Properties of ZnO Thin Films Doped with Ga, Al and (Al+Ga). *J. Alloy Compd.* **2017**, *725*, 1238-1243.
29. Muchuweni, E.; Sathiaraj, T. S.; Nyakotyo, H. Low Temperature Synthesis of ZnO Nanowires on Gazo Thin Films Annealed at Different Temperatures for Solar Cell Application. *Mater. Sci. Semicond. Proc.* **2017**, *68*, 80-86.
30. Berbenni, V.; Milanese, C.; Bruni, G.; Marini, A. Thermal Decomposition of Gallium Nitrate Hydrate $Ga(NO_3)_3 \times xH_2O$. *J. Therm. Anal. Calorim.* **2005**, *82*, 401-407.
31. Viezbicke, B. D.; Patel, S.; Davis, B. E.; Birnie Iii, D. P. Evaluation of the Tauc Method for Optical Absorption Edge Determination: ZnO Thin Films as a Model System. *phys. status solidi (b)* **2015**, *252*, 1700-1710.
32. Parize, R.; Garnier, J.; Chaix-Pluchery, O.; Verrier, C.; Appert, E.; Consonni, V. Effects of Hexamethylenetetramine on the Nucleation and Radial Growth of ZnO Nanowires by Chemical Bath Deposition. *J. Phys. Chem. C* **2016**, *120*, 5242-5250.
33. Villafuerte, J.; Sarigiannidou, E.; Donatini, F.; Kioseoglou, J.; Chaix-Pluchery, O.; Pernot, J.; Consonni, V. Modulating the Growth of Chemically Deposited ZnO Nanowires and the Formation of Nitrogen- and Hydrogen-Related Defects Using pH Adjustment. *Nanoscale Adv.* **2022**, *4*, 1793-1807.
34. Valtiner, M.; Borodin, S.; Grundmeier, G. Stabilization and Acidic Dissolution Mechanism of Single-Crystalline ZnO(0001) Surfaces in Electrolytes Studied by in-Situ Afm Imaging and Ex-Situ Leed. *Langmuir* **2008**, *24*, 5350-5358.
35. Kunze, C.; Valtiner, M.; Michels, R.; Huber, K.; Grundmeier, G. Self-Localization of Polyacrylic Acid Molecules on Polar ZnO(0001)-Zn Surfaces. *Phys. Chem. Chem. Phys.* **2011**, *13*, 12959-12967.
36. Verrier, C.; Appert, E.; Chaix-Pluchery, O.; Rapenne, L.; Rafhay, Q.; Kaminski-Cachopo, A.; Consonni, V. Tunable Morphology and Doping of ZnO Nanowires by Chemical Bath Deposition Using Aluminum Nitrate. *J. Phys. Chem. C* **2017**, *121*, 3573-3583.

37. Sallet, V.; Sartel, C.; Hassani, S.; Vilar, C.; Amiri, G.; Lusson, A.; Jomard, F.; Galtier, P.; Lefebvre, I.; Delerue, C.; Hamza, M.K.; Canut, B.; Masenelli, B. Crystal Facet Engineering in Ga-Doped ZnO Nanowires for Mid-Infrared Plasmonics. *Cryst. Growth Des.* **2018**, *18*, 4287-4295.
38. Demchenko, D. O.; Earles, B.; Liu, H. Y.; Avrutin, V.; Izyumskaya, N.; Özgür, Ü.; Morkoç, H. Impurity Complexes and Conductivity of Ga-Doped ZnO. *Phys. Rev. B* **2011**, *84*, 075201.
39. T-Thienprasert, J.; Rujirawat, S.; Klysubun, W.; Duenow, J. N.; Coutts, T. J.; Zhang, S. B.; Look, D. C.; Limpijumnong, S. Compensation in Al-Doped ZnO by Al-Related Acceptor Complexes: Synchrotron X-Ray Absorption Spectroscopy and Theory. *Phys. Rev. Lett.* **2013**, *110*, 055502.
40. Al-Asedy, H. J.; Bidin, N.; Abbas, K. N.; Al-Azawi, M. A. Structure, Morphology and Photoluminescence Attributes of Al/Ga Co-Doped ZnO Nanofilms: Role of Annealing Time. *Mater. Res. Bull.* **2018**, *97*, 71-80.
41. Serykh, A. I.; Amiridis, M. D. In-Situ X-Ray Photoelectron Spectroscopy Study of Supported Gallium Oxide. *Surf. Sci.* **2010**, *604*, 1002-1005.
42. Feliu, S.; Barranco, V. XPS Study of the Surface Chemistry of Conventional Hot-Dip Galvanised Pure Zn, Galvanneal and Zn–Al Alloy Coatings on Steel. *Acta Mater.* **2003**, *51*, 5413-5424.
43. Cusco, R.; Alarcon-Llado, E.; Ibanez, J.; Artus, L.; Jimenez, J.; Wang, B. G.; Callahan, M. J. Temperature Dependence of Raman Scattering in ZnO. *Phys. Rev. B* **2007**, *75*, 165202.
44. Bundesmann, C.; Ashkenov, N.; Schubert, M.; Spemann, D.; Butz, T.; Kaidashev, E. M.; Lorenz, M.; Grundmann, M. Raman Scattering in ZnO Thin Films Doped with Fe, Sb, Al, Ga, and Li. *Appl. Phys. Lett.* **2003**, *83*, 1974-1976.
45. Manjón, F. J.; Marí, B.; Serrano, J.; Romero, A. H. Silent Raman Modes in Zinc Oxide and Related Nitrides. *J. Appl. Phys.* **2005**, *97*, 053516.
46. Lavrov, E. V.; Weber, J.; Borrnert, F.; Van de Walle, C. G.; Helbig, R. Hydrogen-Related Defects in ZnO Studied by Infrared Absorption Spectroscopy. *Phys. Rev. B* **2002**, *66*, 165205.
47. Lavrov, E. V. Infrared Absorption Spectroscopy of Hydrogen-Related Defects in ZnO. *Physica B* **2003**, *340*, 195-200.
48. Herklotz, F.; Hupfer, A.; Johansen, K. M.; Svensson, B. G.; Koch, S. G.; Lavrov, E. V. Infrared Absorption on a Complex Comprising Three Equivalent Hydrogen Atoms in ZnO. *Phys. Rev. B* **2015**, *92*, 155203.
49. Villafuerte, J.; Chaix-Pluchery, O.; Kioseoglou, J.; Donatini, F.; Sarigiannidou, E.; Pernot, J.; Consonni, V. Engineering Nitrogen- and Hydrogen-Related Defects in ZnO Nanowires Using Thermal Annealing. *Phys. Rev. Mater.* **2021**, *5*, 056001.
50. Nakrela, A.; Benramdane, N.; Bouzidi, A.; Kebbab, Z.; Medles, M.; Mathieu, C. Site Location of Al-Dopant in ZnO Lattice by Exploiting the Structural and Optical Characterisation of ZnO:Al Thin Films. *Res. Phys.* **2016**, *6*, 133-138.
51. Burstein, E. Anomalous Optical Absorption Limit in InSb. *Phys. Rev.* **1954**, *93*, 632-633.
52. Moss, T. S. The Interpretation of the Properties of Indium Antimonide. *Proc. Phys. Soc. Sect. B* **1954**, *67*, 775-782.
53. Brochen, S.; Feuillet, G.; Santailler, J. L.; Obrecht, R.; Lafossas, M.; Ferret, P.; Chauveau, J. M.; Pernot, J. Non-Metal to Metal Transition in N-Type ZnO Single Crystal Materials. *J. Appl. Phys.* **2017**, *121*, 095704.
54. Ye, J. D.; Gu, S. L.; Zhu, S. M.; Liu, S. M.; Zheng, Y. D.; Zhang, R.; Shi, Y. Fermi-Level Band Filling and Band-Gap Renormalization in Ga-Doped ZnO. *Appl. Phys. Lett.* **2005**, *86*, 192111.
55. Frodason, Y. K.; Johansen, K. M.; Bjorheim, T. S.; Svensson, B. G.; Alkauskas, A. Zn Vacancy-Donor Impurity Complexes in ZnO. *Phys. Rev. B* **2018**, *97*, 104109.
56. Yamamoto, T.; Katayama-Yoshida, H. Physics and Control of Valence States in ZnO by Codoping Method. *Physica B* **2001**, *302-303*, 155-162.
57. Johansen, K. M.; Vines, L.; Bjørheim, T. S.; Schifano, R.; Svensson, B. G. Aluminum Migration and Intrinsic Defect Interaction in Single-Crystal Zinc Oxide. *Phys. Rev. Appl.* **2015**, *3*, 024003.